

## Research Article

# Hybrid Numerical Investigation on Soil-Hammer Interaction during Dynamic Compaction

Jian Wang <sup>1,2,3</sup>, Yinghui Cui,<sup>4</sup> and Qimin Li<sup>5</sup>

<sup>1</sup>School of Civil Engineering, Southwest Jiaotong University, Chengdu 610031, China

<sup>2</sup>MOE Key Laboratory of High-Speed Railway Engineering, Southwest Jiaotong University, Chengdu 610031, China

<sup>3</sup>National Engineering Laboratory for Technology of Geological Disaster Prevention in Land Transportation, Southwest Jiaotong University, Chengdu 610031, Sichuan, China

<sup>4</sup>China Academy of Railway Sciences Corporation Limited, Beijing 100081, China

<sup>5</sup>School of Water Resources and Environment, China University of Geoscience (Beijing), Beijing 100083, China

Correspondence should be addressed to Jian Wang; crest01@qq.com

Received 3 May 2019; Revised 21 July 2019; Accepted 24 July 2019; Published 28 August 2019

Academic Editor: Chiara Bedon

Copyright © 2019 Jian Wang et al. This is an open access article distributed under the Creative Commons Attribution License, which permits unrestricted use, distribution, and reproduction in any medium, provided the original work is properly cited.

To investigate the mechanism of hammer-soil interaction under the action of dynamic compaction (DC) on a coarse-grained soil foundation, based on the theory of projectile penetration, the continuous-discrete coupling method is used to simulate the hammer-soil interaction process with different hammer shapes and different particle radii. The physical phenomena and mechanical parameters presented by the hammers and soil particles are quantitatively analyzed. The results show that the penetrating ability of the hammer is proportional to its lateral extrusion shearing ability and inversely proportional to its vertical extrusion capacity. The convex-bottomed hammer has the maximum penetration and lateral extrusion capability, the flat-bottomed hammer has the smallest penetration ability and the lateral extrusion capacity, and the concave-bottomed hammer has a penetration and lateral extrusion ability between those of the convex- and flat-bottomed hammers. The impact strength and vertical disturbance of the flat-bottomed hammer are the strongest, followed by the concave-bottomed hammer and the convex-bottomed hammer. In addition, it is found that the smaller the particle size of the coarse-grained soil is, the greater the depth of the crater formed and the smaller the contact force and the influence range of vertical disturbance. These research results reveal the interaction mechanisms of different hammer types and coarse-grained soil, which is expected to provide reference and guidance for the design and construction of coarse-grained soil foundations enhanced by DC.

## 1. Introduction

Soil-tool interaction is one of the major problems in the fields of civil and agricultural engineering. The soil-tool interaction involves two aspects: one is the force exerted by the tool on the soil and the other is the dynamic response of the soil under the action of the tool. Currently, there are three methods for studying soil-tool interactions [1]: analytical methods, experimental methods, and numerical simulation methods. Due to the geometric irregularity of the shape of the tool and the nonuniformity of the soil fabric, it is difficult to accurately describe the interaction using analytical methods or empirical formulas. Therefore, numerical simulation is generally used to optimize the shape of the

tool, and the test method is used for performance testing after being verified by experimental results. The simulation methods for studying soil-tool interactions can be divided into finite element methods based on the continuum hypothesis [2, 3], discrete element methods based on granular mechanisms [4–8], and continuous-discrete coupling methods [9, 10] considering soil particle properties and tool properties. The finite element method can simulate the shape of the tool and its force characteristics in the continuous domain, so it is mostly used for the optimization design of the tool, but it cannot simulate the compaction effect of the soil and the interaction between the soil particles. The discrete element method can simulate the motion and force characteristics of the soil particles on a mesoscale, but it is

not able to simulate the force characteristics of the tool. The continuous-discrete coupling method can combine the advantages of the finite element and discrete element to overcome the shortcomings of a single simulation method, and it can reflect the soil-tool interaction from the physical essence; thus, it is the most ideal method to study the soil-tool interaction. Dynamic compaction (DC) is a widely applicable soil ground treatment method, and the interaction between hammer and soil is a typical soil-tool interaction problem in the process of dynamic consolidation.

As far as the numerical simulation of DC is concerned, Pan and Selby [11] simulated the DC of loose soils under dynamic loads numerically using the finite element package ABAQUS and summarized the influence of drop height, drop mass, and soil properties on the peak particle acceleration, mass penetration (crater depth), and influenced zone. Liu et al. [12] simulated high-energy tamping using two-dimensional and three-dimensional finite element models and found that the 3D model can simulate the deformation of the foundation better than the 2D model. Gu and Lee [12] analyzed the mechanics of dynamic compaction using a two-dimensional finite element method and found that there were two approaches to increase the depth of improvement, enhancing the energy transfer between the tamper and ground and deepening the zone of transient  $K_0$  compression to delay the spherical dispersion of the stress wave. Wang et al. [13] proposed a simplified model for describing the ground deformation of granular soils caused by dynamic compaction using the dynamic finite element package LS-DYNA to determine the optimal number of blows under DC. Zhou and Song [15] simulated the DC of highly filled foundations filled with broken rock-soil mixtures with the discrete element package PFC3D and investigated the influence of particle shape and fine grain contents on the compaction. Ma et al. [16] simulated the DC process of gravel soil ground by the particle flow discrete element code PFC2D and analyzed the improvement effect and the influence depth of the dynamic compaction of the gravel soil foundation based on the porosity variation. Jia et al. [10] presented a 2D PFC/FLAC coupled method to simultaneously reveal the macro- and micromechanisms of granular soils during dynamic compaction. Li et al. [17] analyzed the influence of particle breakage on DC for gravel soil ground by 3D PFC. Wang and Li [18] investigated the compaction effect and environmental impact effect of DC using a 3D continuous-discrete coupling method.

At present, the DC of a foundation develops in two directions: improving the effect of slamming reinforcement and controlling the environmental impact. Simply relying on increased slamming energy to improve the strength of the strong tamping will increase the adverse noise and vibration effects on the environment. In general, the shape of the hammer affects the force characteristics of the soil-hammer interaction, which has a corresponding degree of influence on the soil upon which the hammer acts. Therefore, optimizing the shape of the hammer is one of the main research tasks of the soil-hammer interaction [4]. The shape of the hammer will also affect the slamming performance and environmental vibration intensity. At

present, the influence of the shape of the hammer on the effect of DC has not been systematically studied and specifically discussed.

To reveal the influence of different shapes of hammers on the consolidation effect and vibration range of coarse-grained soil foundations, this paper intends to simulate the DC process of a coarse-grained soil foundation by a three-dimensional continuous-discrete coupling method and analyze the deformation characteristics and mechanisms of hammer-soil interaction. In this paper, the continuous-discrete coupling model is established based on the laboratory model test. Then, the micromechanical parameters of the particles are obtained by the triaxial shear test simulation results. The reliability of the continuous-discrete coupling model is verified by the laboratory dynamic compaction test results. Finally, the hammer-soil interaction characteristics of different types of hammers, such as flat-bottomed hammers, concave-bottomed hammers, and convex-bottomed hammers, were simulated, and the influence of particle size on the slamming effect was analyzed.

## 2. Continuous-Discrete Coupling (CDC) Methods

Continuous-discrete coupling can use either a complex coupling domain model in which a continuous zone and a discrete zone have overlapping regions or a simple coupling domain model in which a continuous zone and a discrete zone coincide only at the contact surface [19]. This paper uses a coupling method that generates a wall of a discrete model directly from the zone faces of a solid element in a continuous domain [20]. The interfaces between the solid zone and soil particles are composed of two parts: a hammer-soil interface and a box-soil interface. The velocity and displacement of the box element nodes are applied to the soil particles as the velocity and displacement boundary conditions in the discrete domain. At the same time, the force and moment inside the zone element are transferred to the vertex of the solid element through the wall of the discrete model as the stress boundary condition of the hammer and the box in the continuous domain. Based on the principle and method of phenomenological simulation, it is necessary to select the experimental results to verify the numerical calculation. In this paper, the numerical model verification is mainly based on the indoor dynamic compaction model test results of a coal gangue foundation completed by Zhang and Wang [21, 22].

As shown in Figure 1(a), the box is a cylinder with an outer diameter of 0.510 m, an inner diameter of 0.410 m, and an inner depth of 1.0 m. The box model consists of 2384 8-node linear brick elements (C3D8). The hammer is a convex-bottomed cylinder with 0.232 m height and 0.22 m diameter. It consists of 3000 C3D8 elements. Both the hammer and the box are made of steel with a modulus of elasticity of 200 GPa, a Poisson's ratio of 0.25, and a density of 7850 kg. The mass of the hammer is 25 kg. To avoid the convergence problem caused by the excessive difference in stiffness between steel and soil particles in the continuous-discrete coupling

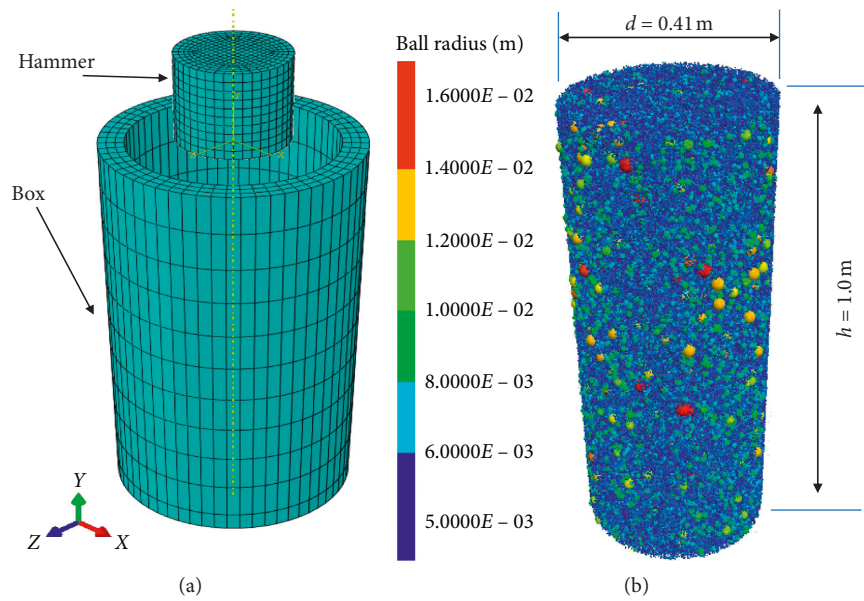


FIGURE 1: (a) Full-scale hammer and box models in the continuous domain; (b) the DEM model replicating the particle size distribution of laboratory tests.

calculation, the elastic modulus of the steel is set to 80 MPa in the actual calculation.

In a micromechanical simulation method, discrete elements can generate a true grading distribution of particle assemblies. At the macroscopic scale, if the particles are actually graded to form particles, the number of particles can reach more than one million, which will cause difficulties in conventional mechanical calculations. There are two current solutions: one is to study the physical and mechanical properties of the true gradation particle set in a local area by mesoscope coupling; the other is to simplify the particle size distribution and reduce the number of calculated model particles to less than two hundred thousand by using uniform particle size distribution so that it is suitable for calculation in small workstations. In this paper, the micromechanical parameters calibration and CDC model validation are performed using the particle size distribution which resembles coal gangue foundation fillings in the laboratory test [22]. After that, CDC models with uniform particle sizes are used to analyze the effect of the shape of the tampers and the particle sizes on the DC effect for simplification. As shown in Figure 1(b), the DEM model used for DC validation is a cylindrical column with diameter 0.41 m and height 1.0 m and the particle diameters are between 1 mm and 32 mm. Specifically, the particle content in the range of 1 mm–5 mm, 5 mm–13 mm, 13 mm–26 mm, and 26 mm–32 mm is 45%, 33%, 17%, and 5%, respectively. The resulted grain size distribution curve of DEM simulations is very close to that of the laboratory test (Figure 2).

The discrete model is made up of granular material with a certain bond strength to simulate the coal gangue. Therefore, the discrete particle model uses a linear contact bond model [23], and the interaction between particles is simplified to a combination of normal and tangential springs, sliders, and dampers; there is a certain shear and

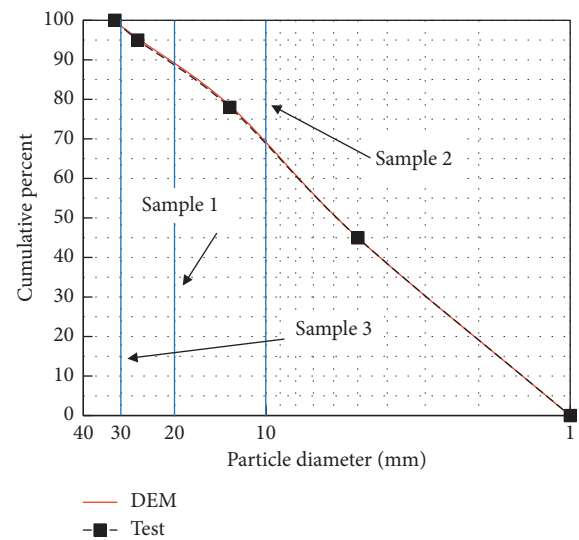


FIGURE 2: Grain size distribution of the laboratory test and DEM simulations.

tensile strength between particles. Without considering the geometry and using a back-analysis method [18, 24], the discrete elements consist of spherical particles with an elastic modulus of 80 MPa, a normal to tangential stiffness ratio of 2.0, a friction coefficient of 0.6, a tensile strength of 20 kPa, and a shear strength of 200 kPa (Table 1).

### 3. Parameter Determination and Model Validation

*3.1. Relationship between Mesoscopic and Macroscopic Parameters.* Triaxial tests [25] can be used to establish the relationship between the macroscopic mechanical

TABLE 1: Micromechanical parameters used in DEM (PFC3D).

Parameter type	Ball-ball	Ball-wall
Density $\rho$ ( $\text{kg}\cdot\text{m}^{-3}$ )	2600	
Contact modulus $E_c$ (Pa)	$8.0 \times 10^7$	$8.0 \times 10^7$
Ratio of stiffness $k_n/k_s$	2	2
Normal critical damping ratio	0.9	1
Shear critical damping ratio	0.9	
Tensile strength (Pa)	$2.0 \times 10^4$	
Cohesion (Pa)	$2.0 \times 10^5$	
Porosity	0.4	
Frictional coefficient	0.6	0.01

parameters of the coal gangue and its mesoscopic parameters. If we know the mesoscopic parameters, we can obtain the corresponding macroscopic parameters directly by means of a triaxial test. Otherwise, we should carry out a number of triaxial tests on discrete samples with assumed mesoscopic properties to achieve results close to the preferred response of the actual material. The test curves are shown in Figure 3(a). The triaxial test model consists of top and bottom platens, a cylindrical membrane, and particles. The cylinder of the DEM model is 300 mm high and has a radius of 100 mm. There are 140877 particles generated with grain size distribution shown in Figure 2. The particle parameters are as indicated above. Confining pressures of 0 kPa, 10 kPa, 50 kPa, and 100 kPa were applied by a servo mechanism separately, and the top platen and bottom platen were slowly moved toward each other at a speed of 0.003 mm/s until the radial strain of the model exceeded 1%. Macroscopic mechanical parameters can be obtained by a triaxial test simulation of granular materials and vice versa [18, 24]. The triaxial test strength envelope and its fitting result are shown in Figure 3(b). Through least square fitting, the macroscopic material corresponding to the micromechanical parameters of the particles has an internal friction angle of  $57.32^\circ$  and a cohesive strength of 143.4 kPa.

**3.2. Validation of the CDC Model.** Based on phenomenological theory and phenomenological simulation, the main function of numerical calculation is description and prediction, and the calculation of parameter verification is the basis for testing the rationality of numerical calculation results. For DC simulations, the reliability of numerical simulations of the depth of the crater and soil dynamic stress distributions can be used. In accordance with the verification method described by Coetzee [26], this paper uses the soil dynamic test results to verify the model calculation results. When the tamping energy is 200 N·m (i.e., the 25 kg hammer is dropped from the height of 0.8 m), laboratory test results and simulated results are shown in Figure 4. Comparing the test values with the simulated values, it is found that both of the vertical soil dynamic stress amplitudes are equivalent (approximately 279 kPa), and the shapes of the soil dynamic stress curves are similar. At the same time, the calculated crater depth is 1.5 cm, which is very close to the test result of 1.8 cm. Thus, the continuous-discrete coupled numerical

calculation can reproduce the indoor DC test process and make a reasonable prediction of the impact of slamming parameter changes.

## 4. Results and Discussion

### 4.1. Influence of Hammer Shape on DC

**4.1.1. Types of Hammer Analyzed.** There are three main types of hammers: flat-bottomed cylinders, spherical cap-shaped convex-bottomed cylinders, and spherically shaped concave-bottomed cylinders, as shown in Table 2. All three types of hammers are 25 kg and fall from the same height of 0.8 m. Both the radius and the height of the convex and the concave spherical caps are 510.1667 and 12 mm, respectively. Compared with the hammer simulated by the discrete particles by Ma et al. [16], the shape of the hammer simulated by the solid element is more accurate and easier to control, which is more in line with the actual situation.

### 4.1.2. Character of Hammer Stress and Particle Displacement.

On the basis of the CDC model with actual grain size distribution having been validated by the laboratory test, a simplified DEM model with uniform radius of 10 mm (labeled as sample 1 in Figure 2) is adopted, which is assembled by 10191 particles in the cylindrical box as shown in Figure 1(a) and thus with an acceptable time consumption for numerical simulation.

The displacement isogram of soil particles and the force diagram of the smashing hammer at the moment of maximum contact force for the flat-bottomed hammer (i.e.,  $t = 3.7$  ms) and the completion time of the compaction (i.e.,  $t = 15$  ms) are shown in Figures 5(a)–5(f). When  $t = 3.7$  ms, the crater depths  $\Delta h$  under the action of the flat-bottomed hammer, concave-bottomed hammer, and convex-bottomed hammer are 8.0 mm, 11.5 mm, and 13.0 mm, respectively. At the same time, the depths of particle disturbance caused by the compact action of the flat-bottomed hammer, concave-bottomed hammer, and convex-bottomed hammer are 430 mm, 335 mm, and 333 mm, respectively, as shown in Figures 5(a)–5(c). When  $t = 15$  ms, the crater depths for the hammer-soil interaction of the flat-bottomed hammer, concave-bottomed hammer, and convex-bottomed hammer are 8.5 mm, 12.3 mm, and 16.6 mm, respectively, as shown in Figures 5(d)–5(f). Meanwhile, the corresponding turbulence depths of these three hammers are 840 mm, 825 mm, and 820 mm, respectively. Under the same slamming energy, the crater caused by the flat-bottomed hammer is the shallowest, but the depth of the disturbance is the largest. The crater caused by the convex-bottomed hammer is the deepest, but its disturbance depth is the smallest. Both the crater depth and the disturbance depth caused by the concave-bottomed hammer range between the other hammers. According to the test results [27], when the hammer acts on the granular soil, the particles under the bottom of the hammer will undergo vertical or lateral extrusion, forming a lateral shear zone and a vertical compression zone. The penetration

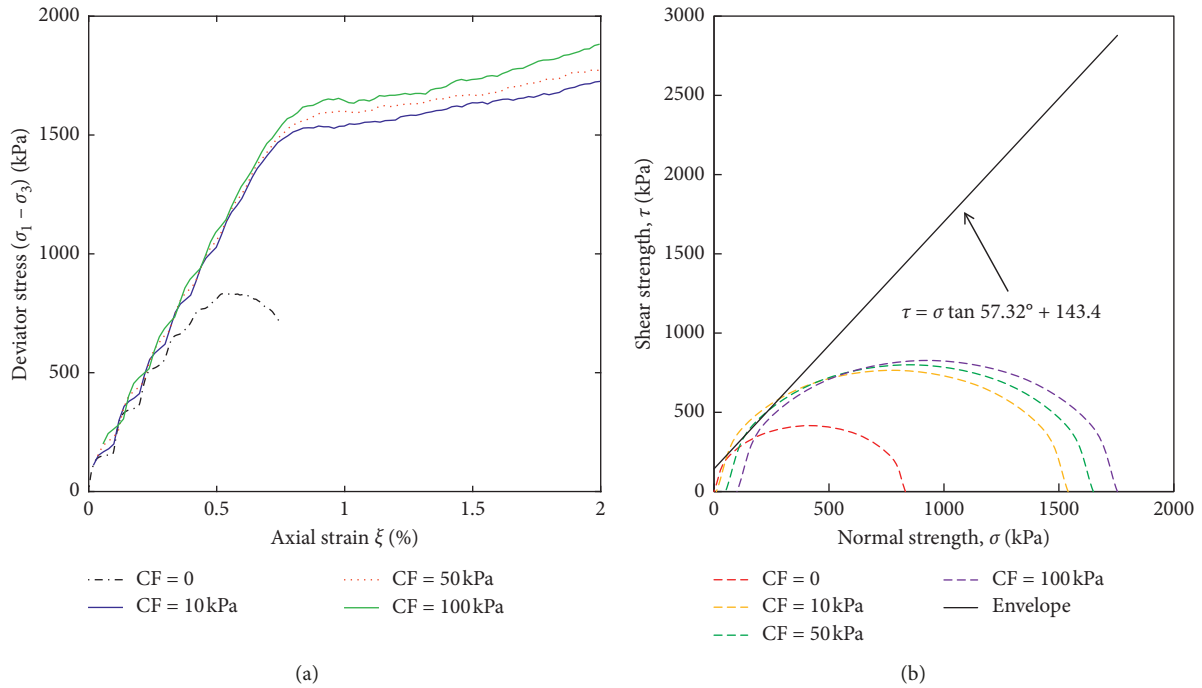


FIGURE 3: Triaxial tests of soil particles of (a) the triaxial test curves with confining pressures of 0, 10, 50, and 100 kPa and (b) the triaxial test strength envelope and its fitting results.

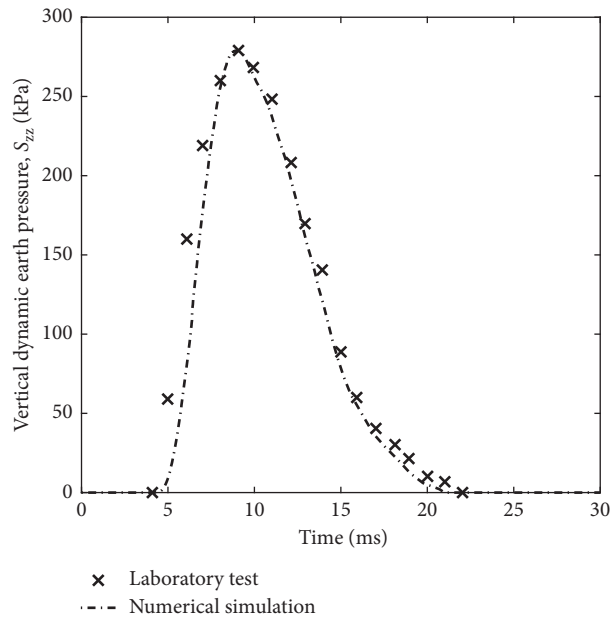


FIGURE 4: Time history of vertical dynamic stress.

depths of the convex-bottomed hammer and the concave-bottomed hammer are greater than those of the flat-bottomed hammer, but at the same time, the lateral squeezing action of the convex-bottomed hammer and the concave-bottomed hammer on the granules are more significant than those of the flat-bottomed hammer, thus affecting the vertical reinforcement effect. It can be seen from the comparison of Figures 5(a)–5(c) and 5(d)–5(f) that the

slamming effect of the three different bottomed hammers has the same trend at different times, which means that the boundary effect of the model box does not affect the conclusions of this paper.

In addition, it can be seen that the force characteristics of different hammer shapes are different: the contact stress distribution at the bottom of the flat-bottomed hammer is more uniform; the edge of the concave-bottomed hammer

TABLE 2: Shape of hammers.

Hammer	Geometry	Radius (mm)	Height (mm)	Volume (mm <sup>3</sup> )	Bottom area (mm <sup>2</sup> )
Flat hammer		220	220	8362920	38013
Concave hammer		220	232	8590094	38466
Convex hammer		220	232	8591904	38466

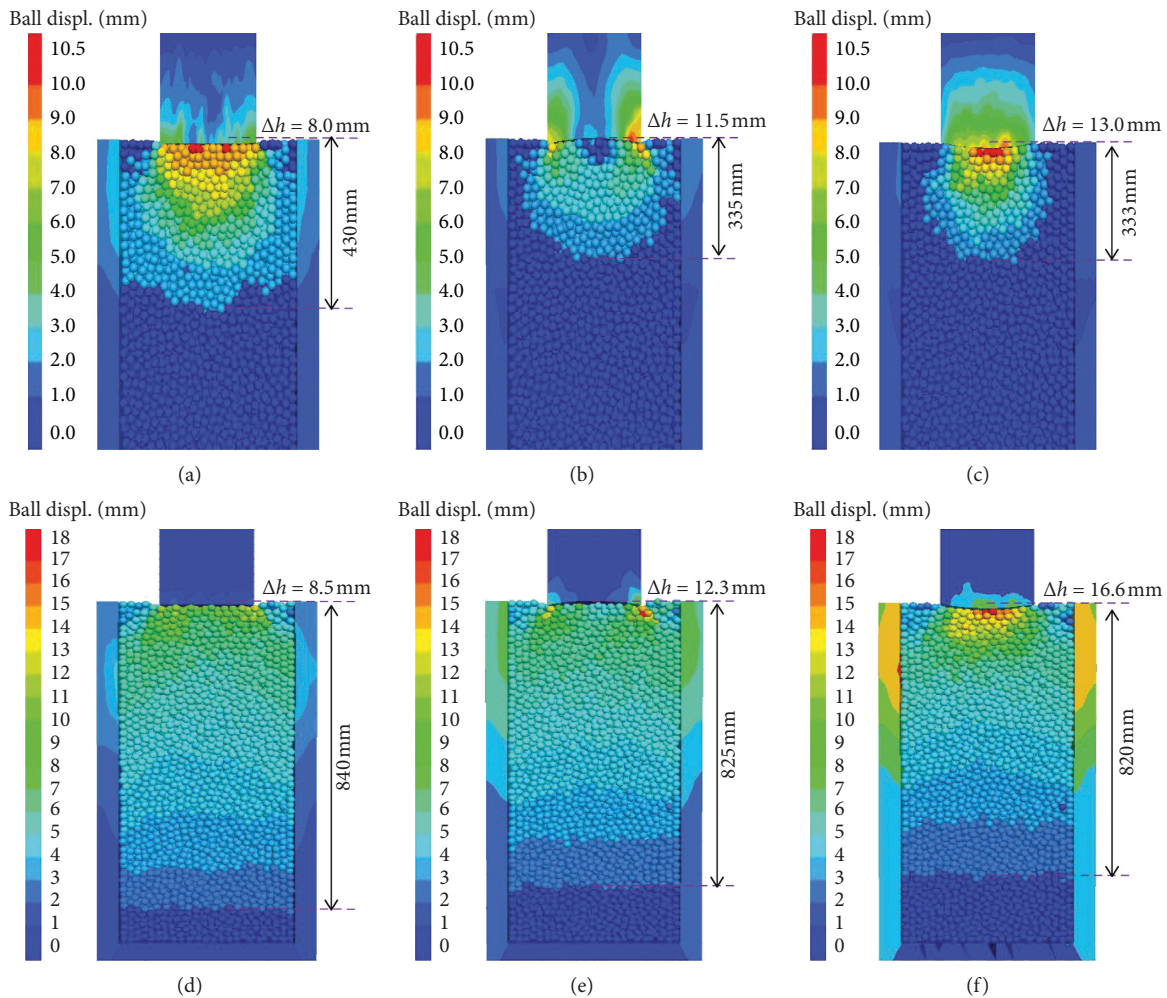


FIGURE 5: Particle displacement punched by (a) flat-bottomed hammer, (b) concave-bottomed hammer, and (c) convex-bottomed hammer at 3.7 ms and particle displacement punched by (d) flat-bottomed hammer, (e) concave-bottomed hammer, and (f) convex-bottomed hammer at 15 ms (the upper parts of hammers are truncated in this figure).

produces a more significant stress concentration phenomenon; the central part of the convex-bottomed hammer produces stress concentration. The above analysis shows that the lateral extrusion of the soil particles is in a competing relation with the vertical extrusion displacement. The penetrating ability of the hammer is proportional to its lateral extrusion shearing ability and inversely proportional to its vertical extrusion capacity. Compared with a flat-

bottomed hammer, a special-shaped hammer, such as a convex-bottomed or concave-bottomed hammer, offers increased penetration ability but weaker vertical disturbance depth.

4.1.3. Analysis of Penetration Characteristics of Hammer. The time-history curves of the flat-bottomed, concave-bottomed, and convex-bottomed hammers are shown in

Figure 6(a). Under the same slamming energy and soil conditions, the displacement of the convex-bottomed hammer is the largest, followed by the concave-bottomed hammer and the flat-bottomed hammer. The displacement of the hammer is consistent with the depth of the crater shown in Figure 4. In addition, it was found that the convex-bottomed hammer has no rebound, the flat-bottomed hammer has a slight rebound (a rebound displacement of approximately 1 mm), and the concave-bottomed hammer has the largest rebound value (a rebound displacement of approximately 2 mm). If the penetration efficiency is defined as the ratio of the penetration depth to the impact velocity of the projectile [28], it can be found that the convex-bottomed hammer has the highest penetration efficiency, the penetration efficiency of the concave-bottomed hammer is in the middle, and the penetration efficiency of the flat-bottomed hammer is smallest, which is similar to the law of projectile penetration [28], as shown in Figure 6(b). At the same time, it can be seen that the penetration efficiency of the tamping hammer increases with increasing penetration depth and penetration speed, indicating that the granular medium around the hammer exhibits quasi-fluidized phenomena during the subsequent penetration process [29], which is more conducive to penetration.

In terms of the contact force of the hammer, the flat-bottomed hammer is the largest, followed by the concave-bottomed hammer, and the convex-bottomed hammer has the smallest contact force, as shown in Figure 6(c). There is a local oscillation phenomenon in the curve of contact force history, indicating that there is a stress localization effect in the hammer-particle contact. In the initial contact with the particles, the contact force of the flat-bottomed hammer rapidly increases to 35.8 kN in a short time of 0.14 ms and then falls back to a second peak of 23.1 kN at  $t_1 = 1.1$  ms, at which time the acceleration of the hammer reaches a maximum value of  $1368 \text{ m/s}^2$ . When  $t_2 = 3.2$  ms, the contact force of the concave-bottomed hammer reaches a maximum value of 22.5 kN and the acceleration of the hammer reaches a maximum value of  $1133 \text{ m/s}^2$ . When  $t_3 = 3.4$  ms, the contact force of the convex-bottomed hammer reaches a maximum value of 19.2 kN and the acceleration of the hammer reaches a maximum value of  $826 \text{ m/s}^2$ . Among the three types of hammers, the peak contact force and the peak acceleration of the flat-bottomed hammer are the largest, the concave-bottomed hammer is the second, and the convex-bottomed hammer is the smallest. In addition, the arrival time of the peak contact force and peak acceleration of the flat bottom hammer are the earliest, followed by the concave-bottomed hammer and the convex-bottomed hammer. The vertical earth pressure history at the bottom of the crater has similar characteristics to the contact force history, as shown in Figure 6(d). When  $t = 3.1$  ms, the vertical earth pressure at the bottom of the crater under the action of the flat-bottomed hammer is 294 kPa. When  $t = 4.5$  ms, the vertical earth pressure at the bottom of the crater under the action of the concave-bottomed hammer is 249 kPa. When  $t = 5.4$  ms, the vertical earth pressure at the bottom of the crater under the action of the convex-

bottomed hammer is 265 kPa. It is clear that the shortest arrival time of the peak vertical earth pressure is achieved by the flat-bottomed hammer, followed by the concave-bottomed hammer and convex-bottomed hammer. In addition, the peak earth pressure at the bottom of the crater appears later than the peak contact force of the hammer, which is consistent with the actual transmission of the contact force to soil particles.

**4.2. Impact of Particle Size on DC.** To study the effect of particle size on the slamming effect, DEM models composed of particles with uniform particle size distribution of 15 mm, 10 mm, and 5 mm radii (labeled as sample 3, sample 1, and sample 1 in Figure 2) at the time of the maximum contact force of flat-bottomed hammer (i.e.,  $t_1 = 1.1$  ms) were selected for analysis. The selection of particle size is based on two considerations: one is that the particle size is within the range of particle size distribution of experimental soil samples; the other is that the number of particles in the generated DEM model should not be too large or too small, which is not only convenient for calculation but also can reflect the mesomechanical behavior of particle assembly. For this cylindrical discrete element model, when the particle radius is 15 mm, 10 mm, and 5 mm, the number of particles generated is 3081, 10191, and 78669, respectively, which meets the above two requirements.

When the particle size is 15 mm, the crater depth  $\Delta h$  is 8.0 mm and the DC disturbance depth is 250 mm, as shown in Figure 7(a). When the particle size is 10 mm, the crater depth  $\Delta h$  is 9.0 mm and the DC effected depth is 245 mm, as shown in Figure 7(b). When the particle size is 5 mm, the crater depth  $\Delta h$  is 38 mm and the effected depth is 220 mm, as shown in Figure 7(c). As the particle size decreases, the depth of the crater increases and the depth of the disturbance decreases. The maximum contact forces between particles with radii of 15 mm, 10 mm, and 5 mm are 583 N, 345 N, and 141 N, respectively (Figures 7(d)–7(f)). It can be seen that the contact force between particles is positively correlated with the dynamic disturbance depth.

The area directly affected by the hammer can be called as localized fluidization zone, where the discrete particles do not steadily contact with each other and behave like a fluid [30]. Experiments had revealed that the smaller the particles, the easier it is to fluidize [31]. Thus, the fluidized zone of the soil around the hammer will increase as the particle size decreases, so that the crater depth also increases as the particle diameter decreases. The area adjacent to the fluidization zone in the DC is called the compaction zone [30]. It has been shown that the larger the particle size, the greater the contact force in the case of the same porosity, friction coefficient, and external load [32, 33]. Based on the correlation between contact force and disturbance depth mentioned above, the range of disturbance, which is only a little bit larger than that of compaction zone, decreases with the decrease of particle size.

It is also found that as the particle size increases, the contact force between the particles increases linearly; while the depth of the crater decreases in a concave curve, the

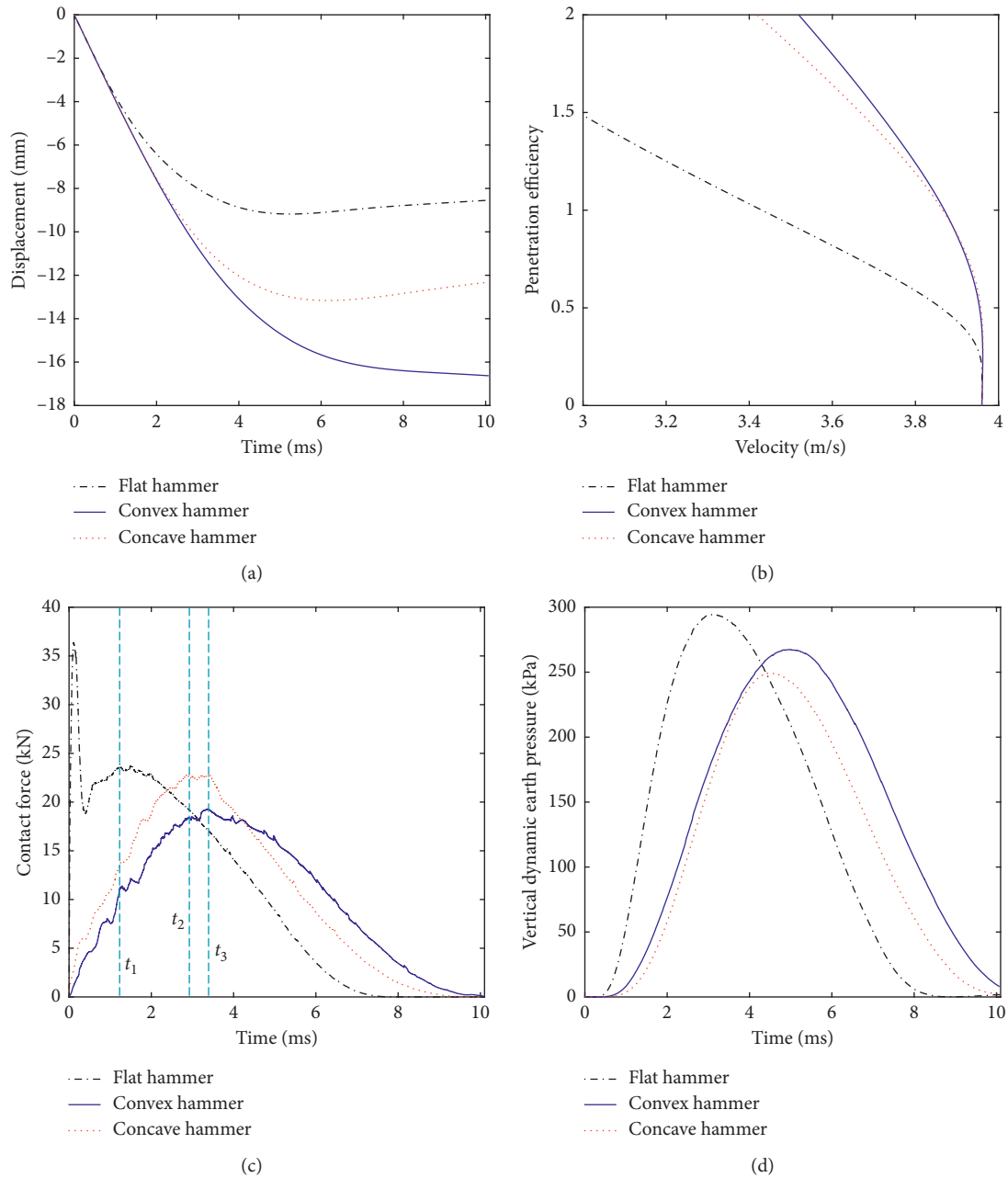


FIGURE 6: Time history of (a) displacement and (b) penetration efficiency, (c) contact force between hammer and soil, and (d) vertical dynamic earth pressure underneath the hammer for flat, convex, and concave hammers.

depth of disturbance increases in a convex curve. The smaller the particle size, the more easily the particles are laterally extruded and the higher the efficiency of the hammer penetration. At the same time, the smaller the particle size is, the smaller the contact force transmitted between the particles and the smaller the vertical disturbance depth. In addition, it is found that for different particle sizes, the stress diffusion angle [34] and lateral displacement caused by hammer action are not much different, which indicates that the particle size mainly affects the depth of the crater and the vertical extrusion depth.

## 5. Conclusions

This paper simulates the hammer-soil interaction process for the first time with the 3D continuous-discrete coupling method to address the influence of hammer shape and particle size on the penetration and densification effect for coarse-grained soil foundations. Similar to our former work [18], the stone backfill was simulated by particles in a discrete domain, the test box and tamping hammer were modeled by solid elements in a continuous domain, and the soil-box interface and soil-hammer interface were simulated

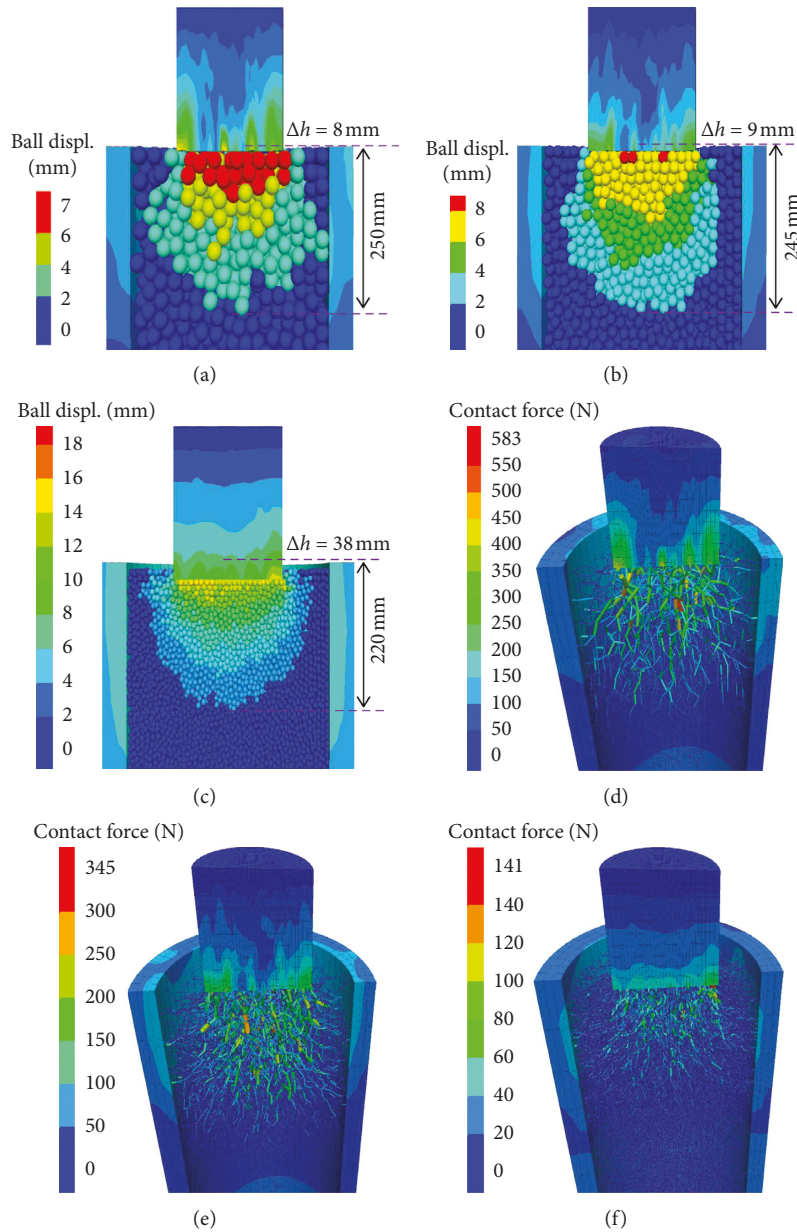


FIGURE 7: Particle displacement diagram with radius of (a) 15 mm, (b) 10 mm, and (c) 5 mm; particle contact force chain diagram with radius of (d) 15 mm, (e) 10 mm, and (f) 5 mm under the action of a flat-bottomed hammer.

by an edge-to-edge coupling scheme. The coupling model accounts for the physical nature of the stone backfill, test box, and hammer. During the interaction process, the behavior of the hammer and the response of soil particles impacted by the hammer can be restored quantitatively by the coupling method. The following conclusions can be drawn from the observed results of the coupled continuous-discrete simulation:

- (a) The penetrating ability of the hammer is proportional to its lateral extrusion shearing ability and inversely proportional to its vertical extrusion capacity. Compared with a flat-bottomed hammer, a special-shaped hammer, such as a convex-bottomed

or concave-bottomed hammer, increases the penetrating ability but reduces the depth of disturbance.

- (b) An analysis of the force characteristics of different types of tamping hammers revealed that the arrival time of peak contact force and peak vertical dynamic earth pressure is earliest for the flat-bottomed hammer, followed by the concave-bottomed hammer and convex-bottomed hammer. This means that the impact of the flat-bottomed hammer is the strongest, followed by the concave-bottomed hammer and finally the convex-bottomed hammer.
- (c) Analyzing the discrete model with different sizes of particles, it is revealed that the smaller the particle

size is, the larger the depth of the crater formed and the smaller the contact force and the depth of disturbance. The contact force between particles increases linearly with increasing particle size. The depth of the crater decreases in a concave curve, while the depth of disturbance increases in a convex curve. It is also found that the stress diffusion angle and lateral displacement caused by CD action are not obviously related to particle change.

The proposed continuous-discrete coupling method can reflect the characteristics of the hammer-soil interaction during DC with physical meaning and inspire further studies of soil-structure, soil-tool, and granular-machine interactions. These research results reveal the interaction mechanisms of different types of hammers and coarse-grained soils, which is expected to provide reference and guidance for the design and construction of coarse-grained soil foundations enhanced by DC.

### Data Availability

The data used to support the findings of this study are available from the corresponding author upon request.

### Conflicts of Interest

The authors declare that they have no conflicts of interest.

### Acknowledgments

J. Wang received financial support from the National Natural Science Foundation of China (NSFC: 51308474), Y. Cui received financial support from the National Natural Science Foundation of China (NSFC: 41731288 and 41701088), and Q. Li received financial support from the Key R&D Projects (the High and New Domain) of Shanxi Province in 2018 (no. 201803D121112).

### References

- [1] O. A. Ani, B. B. Uzoejinwa, A. O. Ezeama, A. P. Onwualu, S. N. Ugwu, and C. J. Ohagwu, "Overview of soil-machine interaction studies in soil bins," *Soil and Tillage Research*, vol. 175, pp. 13–27, 2018.
- [2] H. Bentaher, A. Ibrahim, E. Hamza et al., "Finite element simulation of moldboard-soil interaction," *Soil and Tillage Research*, vol. 134, pp. 11–16, 2013.
- [3] M. Ucgul, C. Saunders, and J. M. Fielke, "Comparison of the discrete element and finite element methods to model the interaction of soil and tool cutting edge," *Biosystems Engineering*, vol. 169, pp. 199–208, 2018.
- [4] B. Li, Y. Chen, and J. Chen, "Modeling of soil-claw interaction using the discrete element method (DEM)," *Soil and Tillage Research*, vol. 158, pp. 177–185, 2016.
- [5] V. Milkevych, L. J. Munkholm, Y. Chen, and T. Nyord, "Modelling approach for soil displacement in tillage using discrete element method," *Soil and Tillage Research*, vol. 183, pp. 60–71, 2018.
- [6] I. Shmulevich, "State of the art modeling of soil-tillage interaction using discrete element method," *Soil and Tillage Research*, vol. 111, no. 1, pp. 41–53, 2010.
- [7] J. Wang, Q. Li, C. Yang, Y. Huang, and C. Zhou, "A simple model for elastic-plastic contact of granular geomaterials," *Advances in Materials Science and Engineering*, vol. 2018, Article ID 6783791, 11 pages, 2018.
- [8] J. Wang, Q. Li, C. Yang, and C. Zhou, "Repeated loading model for elastic-plastic contact of geomaterial," *Advances in Mechanical Engineering*, vol. 10, no. 7, pp. 1–11, 2018.
- [9] N. Guo and J. Zhao, "A coupled FEM/DEM approach for hierarchical multiscale modelling of granular media," *International Journal for Numerical Methods in Engineering*, vol. 99, no. 11, pp. 789–818, 2014.
- [10] M. Jia, Y. Yang, B. Liu, and S. Wu, "PFC/FLAC coupled simulation of dynamic compaction in granular soils," *Granular Matter*, vol. 20, no. 4, p. 76, 2018.
- [11] J. L. Pan and A. R. Selby, "Simulation of dynamic compaction of loose granular soils," *Advances in Engineering Software*, vol. 33, no. 7–10, pp. 631–640, 2002.
- [12] H. Liu, S. Zhao, and G. Jia, "FEM analyses of deformations of HELDC-treated macadam foundation under large-scaled oil tank," *Chinese Journal of Geotechnical Engineering*, vol. 32, no. 2, pp. 228–231, 2010.
- [13] Q. Gu and F.-H. Lee, "Ground response to dynamic compaction of dry sand," *Géotechnique*, vol. 52, no. 7, pp. 481–493, 2002.
- [14] W. Wang, J.-J. Chen, and J.-H. Wang, "Estimation method for ground deformation of granular soils caused by dynamic compaction," *Soil Dynamics and Earthquake Engineering*, vol. 92, pp. 266–278, 2017.
- [15] M. Zhou and E. Song, "Particle flow simulations of the compaction of filling materials in highly filled foundation with analyses of the transverse isotropy," *Journal of Tsinghua University (Science and Technology)*, vol. 56, no. 12, pp. 1312–1319, 2016.
- [16] Z.-Y. Ma, F.-N. Dang, and H.-J. Liao, "Numerical study of the dynamic compaction of gravel soil ground using the discrete element method," *Granular Matter*, vol. 16, no. 6, pp. 881–889, 2014.
- [17] X. Li, J. Li, X. Ma, J. Teng, and S. Zhang, "Numerical study of the dynamic compaction process considering the phenomenon of particle Breakage," *Advances in Civil Engineering*, vol. 2018, Article ID 1838370, 10 pages, 2018.
- [18] J. Wang and Q. Li, "Coupled continuum-discrete modeling of rammed floating stone column installation," *AIP Advances*, vol. 9, no. 1, Article ID 015222, 2019.
- [19] A. Breugnot, S. Lambert, P. Villard, and P. Gotteland, "A discrete/continuous coupled approach for modeling impacts on cellular geostructures," *Rock Mechanics and Rock Engineering*, vol. 49, no. 5, pp. 1831–1848, 2016.
- [20] Itasca Consulting Group, *FLAC3D—Fast Lagrangian Analysis of Continua*, Itasca Consulting Group, Minneapolis, MN, USA, 2016.
- [21] Q. Zhang and D. Wang, "Model tests on dynamic stress in colliery wastes improved by dynamic compaction," *Chinese Journal of Geotechnical Engineering*, vol. 34, no. 6, pp. 1142–1147, 2012.
- [22] Q. Zhang and D. Wang, "Physical model tests of coal gangue foundation under dynamic compaction loads," *Chinese Journal of Rock Mechanics and Engineering*, vol. 32, no. 5, pp. 1049–1056, 2013.
- [23] D. O. Potyondy and P. A. Cundall, "A bonded-particle model for rock," *International Journal of Rock Mechanics and Mining Sciences*, vol. 41, no. 8, pp. 1329–1364, 2004.
- [24] B. Indraratna, N. T. Ngo, C. Rujikiatkamjorn, and S. W. Sloan, "Coupled discrete element-finite difference method for

- analysing the load-deformation behaviour of a single stone column in soft soil,” *Computers and Geotechnics*, vol. 63, pp. 267–278, 2015.
- [25] J. A. Knappett and R. F. Craig, *Craig’s Soil Mechanics*, Spon Press, Oxford, UK, 8th edition, 2012.
- [26] C. J. Coetzee, “Review: calibration of the discrete element method,” *Powder Technology*, vol. 310, pp. 104–142, 2017.
- [27] Y. Nazhat and D. Airey, “The kinematics of granular soils subjected to rapid impact loading,” *Granular Matter*, vol. 17, no. 1, pp. 1–20, 2015.
- [28] M. Song, X. Wang, X. Zhao et al., “Influencing factors of penetration efficiency for projectiles’ high-speed penetration into concrete targets,” *Journal of Nanjing University of Science and Technology*, vol. 38, no. 3, pp. 390–395, 2014.
- [29] R. C. Hurley, “Force chains, friction, and flow: behavior of granular media across length scales,” in *Engineering and Applied Science*, p. 138, California Institute of Technology, Pasadena, CA, USA, 2016.
- [30] T. Triantafyllidis and I. Kimmig, “A simplified model for vibro compaction of granular soils,” *Soil Dynamics and Earthquake Engineering*, vol. 122, pp. 261–273, 2019.
- [31] O. Roche, M. A. Gilbertson, J. C. Phillips, and R. S. J. Sparks, “The influence of particle size on the flow of initially fluidised powders,” *Powder Technology*, vol. 166, no. 3, pp. 167–174, 2006.
- [32] R. K. Desu and R. K. Annabattula, “Particle size effects on the contact force distribution in compacted polydisperse granular assemblies,” *Granular Matter*, vol. 21, no. 2, p. 29, 2019.
- [33] C. Voivret, F. Radjai, J.-Y. Delenne, and M. S. E. Youssoufi, “Multiscale force networks in highly polydisperse granular media,” *Physical Review Letters*, vol. 102, no. 17, 2009.
- [34] J. Wang, Y. Jiang, H. Ouyang, T. Jiang, M. Song, and X. Zhang, “3D continuum-discrete coupling modeling of soil-hammer interaction under dynamic compaction,” *Journal of Vibroengineering*, vol. 21, no. 2, pp. 348–359, 2019.

